4B13 Fluid Mechanics 2: CFD Assignment 2

Finn O'Connor — foconno1@tcd.ie — 22336740

1 Domain Geometry and Mesh

In computational fluid dynamics (CFD), a refined mesh is vital to ensure accuracy as it captures steep velocity and pressure gradients. This ensures reliable predictions of drag, lift, and flow separation, while also improving numerical stability and solution convergence. For this assignment, the flow field geometry and mesh refinement were inspired by two different sources [1], [2].

The NACA3412 aerofoil geometry was generated and downloaded as a .txt file [3]. It was then imported to ANSYS Design Modeller as a 3D curve and generated into a surface. A C-type domain was constructed with a radius of 15 chord lengths (15c) around the leading edge to minimise farfield effects and flow blockage. Vertical lines were placed at the trailing edge and at 0.25c from the leading edge to improve orthogonality near regions of high curvature and pressure gradients. A Boolean subtraction was applied to define the aerofoil as a solid boundary and the surrounding domain as a fluid region. The domain was divided into six faces to allow local mesh refinement.

In Fluent Meshing, edge sizings and bias factors were applied to generate smaller elements near the leading and trailing edges, while maintaining gradual growth toward the farfield. A quadrilateral face mesh was used to improve accuracy along the aerofoil surface. Hard meshing was applied to farfield boundaries, with soft meshing in complex near-wall regions to maintain smooth transitions. The final mesh had an average surface area of 52.176 m² contained approximately 200,000 elements, with a minimum orthogonal quality above 0.85 and a skewness below 0.25, indicating good mesh quality.

The near-wall mesh was designed to achieve a target $y^+ \approx 1$, ensuring the viscous sublayer was fully resolved. This was achieved with a first-layer height of 0.0063 mm, calculated from Cadence's "Compute Grid Space for a Given Y^+" tool [4].

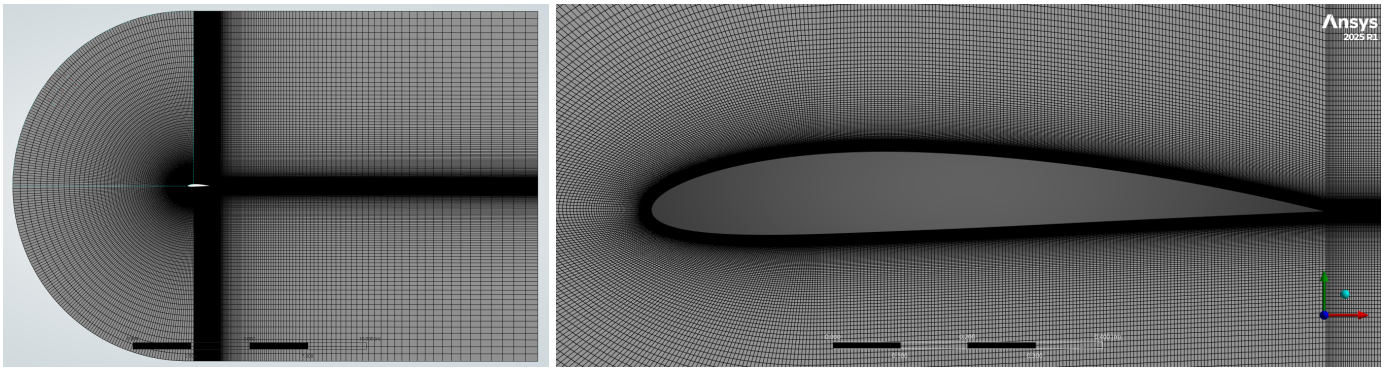

Figure 1: Final mesh used for simulating the NACA3412 simple aerofoil.

Due to the added geometric complexity of the flap, a less-refined mesh was used. The mesh had an average surface area of 111.92 m² and a total of 26916 elements. This was done to ensure that a valid mesh could be generated and inflation layers did not overlap. The first layer thickness of this mesh was 0.003 mm. In theory, this refined mesh compromises the accuracy of pressure gradients, boundary-layer behaviour, separation prediction and force coefficients, but it reduces total compute and avoids inflation-layer conflicts in tight geometric regions.

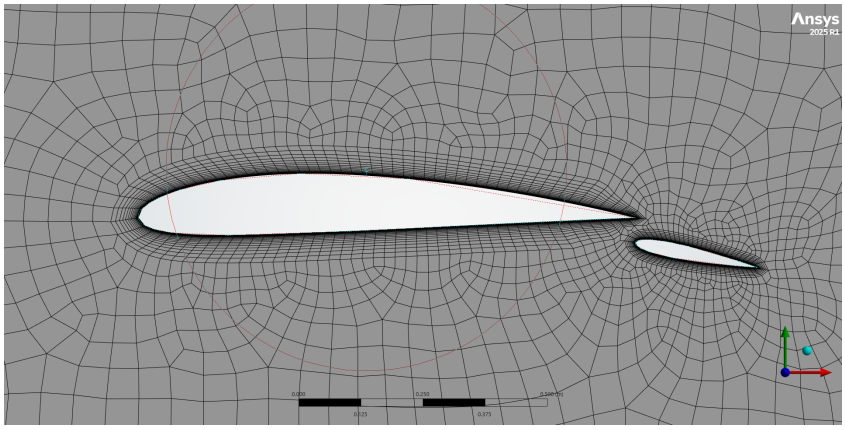

Figure 2: Final mesh used for simulating the NACA3412 flapped aerofoil.

2 Simulation Setup

As experimental data for the NACA3412 aerofoil are not readily available, the NACA2412 profile was used as comparison. Both sections share a 12% thickness and 40% maximum-camber location, but differ in camber (2%, rather than 3%). For comparison in this study, the NACA2412 dataset was used as the primary reference. The Reynolds number, fluid density, and dynamic viscosity values used were 3.1×10^6, $\rho = 1.225$ kg m^{-3}, and $\mu = 1.802 \times 10^{-5}$.

$$Re = \frac{\rho U_\infty L}{\mu} \quad \Rightarrow \quad U_\infty = \frac{\mu Re}{\rho L}, \tag{1}$$

Case	Chord, L (m)	Freestream Velocity, U_∞ (m s^{-1})
Simple aerofoil	1.000	44.87
Flapped aerofoil	1.245	36.63

Named selections were created in Fluent for the aerofoil wall, velocity inlet, and pressure outlet boundaries. The simulations were run using 20 CPU cores and double precision. The SST k-ω turbulence model was selected as it combines accurate near-wall behaviour (from k-ω) with robust freestream performance (from k-ε), making it suitable for aerofoil flows with $y^+ < 1$ and for capturing separation and stall behaviour.

The inlet velocity components were calculated as above for each aerofoil, while the outlet gauge pressure was set to 0 Pa. Reference values were computed from the inlet to ensure correct evaluation of lift and drag coefficients. Hybrid initialization was used to generate a smooth initial flow field and accelerate convergence.

Lift and drag forces, F_L and F_D, were defined as report quantities, with force directions rotated by the angle of attack α. The force direction vectors were specified as:

$$x_{\text{drag}} = \cos\left(\frac{\alpha\pi}{180}\right), \qquad y_{\text{drag}} = \sin\left(\frac{\alpha\pi}{180}\right), \qquad x_{\text{lift}} = -\sin\left(\frac{\alpha\pi}{180}\right), \qquad y_{\text{lift}} = \cos\left(\frac{\alpha\pi}{180}\right) \tag{2}$$

The X and Y forces added as report definitions, which meant the lift and drag forces and coefficients could be calculated. The simulation was run for 2000 iterations, which was sufficient to observe if the solution would converge.

$$F_L = F_y \cos(\alpha) - F_x \sin(\alpha), \qquad F_D = F_y \sin(\alpha) + F_x \cos(\alpha) \tag{3}$$

$$C_L = \frac{F_L}{\frac{1}{2}\rho U_\infty^2 c}, \qquad C_D = \frac{F_D}{\frac{1}{2}\rho U_\infty^2 c} \tag{4}$$

3 Results (Flow Field)

To analyse the aerodynamic behaviour of both aerofoil configurations, the post-processing focused on velocity contours, pressure distributions, and streamline patterns. These plots were used to identify whether the flow remained attached, where suction peaks formed, how the wake developed, and whether any early signs of separation or unsteadiness appeared. By comparing the simple and flapped aerofoils under identical conditions, the aim was to observe how the flap alters the pressure field, accelerates or slows the flow locally, and ultimately affects lift-generation mechanisms from the lowest angles of attack upward.

3.1 Angle of Attack (α) = 0°:

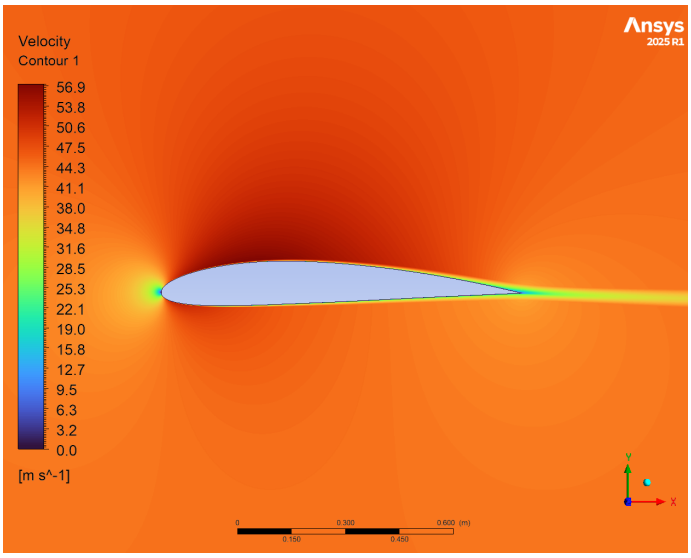

(a) Velocity contour of aerofoil at $\alpha = 0°$

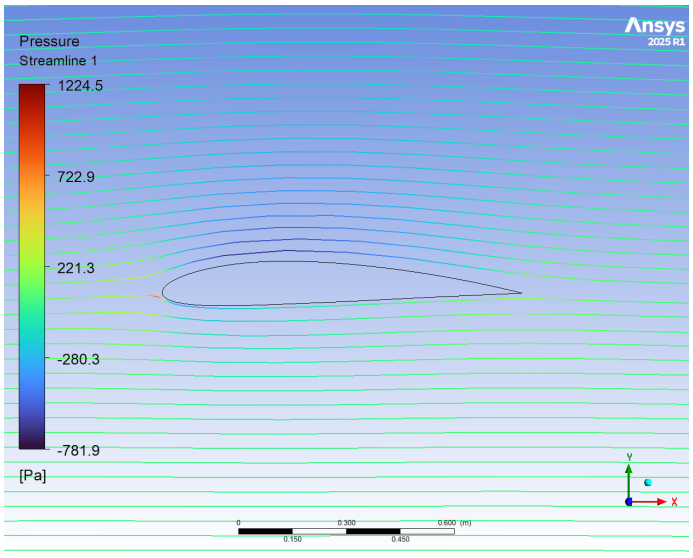

(b) Velocity streamlines of aerofoil at $\alpha = 0°$

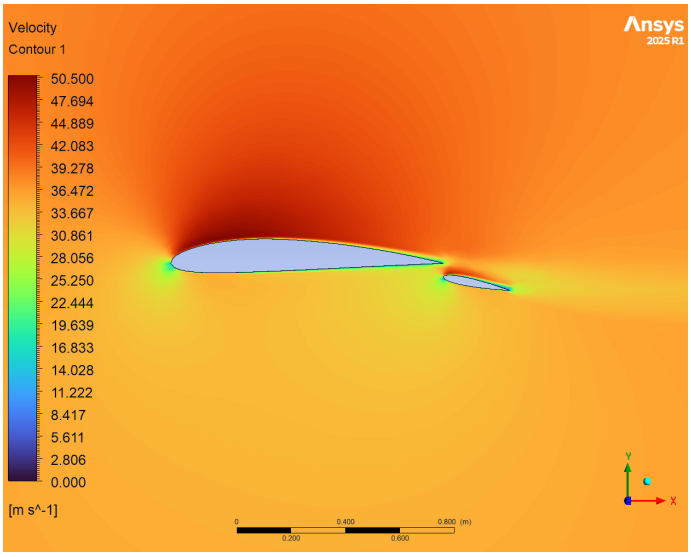

(c) Velocity contour of aerofoil with flap at $\alpha = 0°$

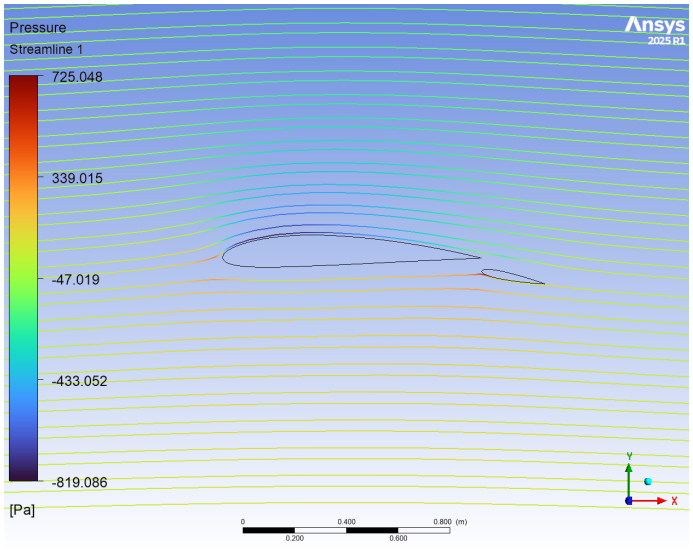

(d) Velocity streamlines of aerofoil with flap at $\alpha = 0°$

Figure 3: Simple and flapped aerofoils positioned at 0°.

At α = 0°, both aerofoils show fully attached flow. For the simple aerofoil, the velocity contour indicates a mild acceleration over the upper surface, producing a small suction region but no separation. The streamlines remain smooth and closely follow the aerofoil shape, and the wake is thin and steady.

For the flapped aerofoil, the flap introduces a stronger local curvature, which increases the acceleration over the upper surface and produces a slightly larger suction peak. The streamlines bend more sharply around the flap but still remain attached, and no recirculation is present. Overall, both geometries behave as expected at zero angle of attack, with stable flow and negligible signs of separation. Convergence was achieved for both (simple at 164 iterations, flap at 213 iterations).

3.2 Angle of Attack (α) = 10°:

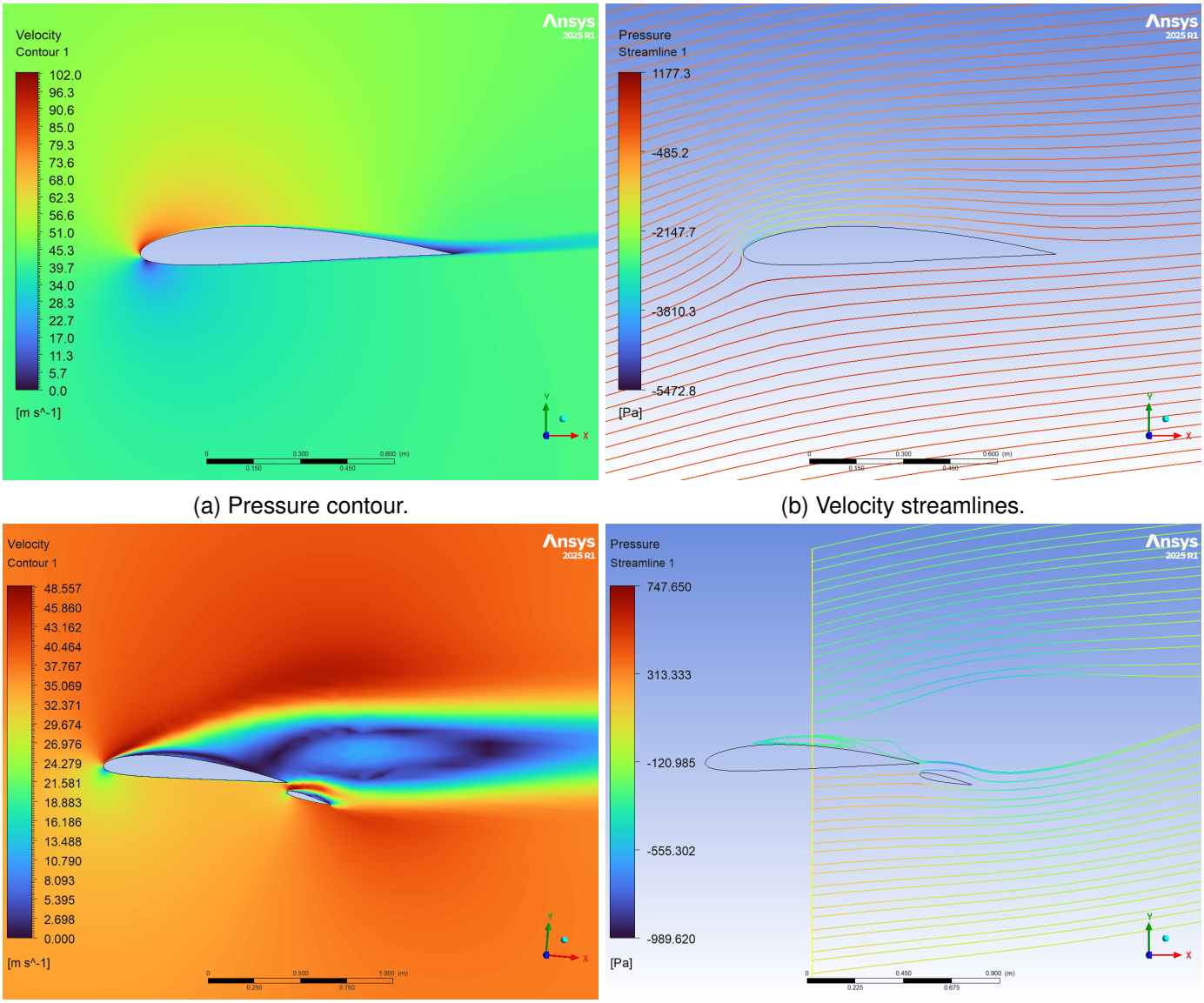

(a) Pressure contour.

(b) Velocity streamlines.

(c) Pressure contour.

(d) Velocity streamlines.

Figure 4: Simple and flapped aerofoils positioned at 10°.

At α = 10°, the simple aerofoil is still in an attached-flow regime. The velocity contour shows a strong acceleration over the upper surface and there is a clear suction region in the pressure plot, with the streamlines following the aerofoil smoothly and leaving a relatively thin wake. This corresponds to a high lift coefficient with only a moderate drag penalty.

For the flapped aerofoil, the suction peak is even stronger, especially over the flap, and the streamlines bend sharply around the hinge. A small separated bubble forms just downstream of the flap, but the main upper-surface flow remains largely attached, so the aerofoil has not yet fully stalled. The residuals and force histories converge much better at this angle than at $16°$, although the flapped case shows slightly more unsteadiness, again reflecting the forming but still limited separation near the flap. The simple aerofoil converged after 324 iterations, while the flapped aerofoil did not converge residually, but did achieve some degree of convergence in the force results.

3.3 Angle of Attack (α) = 16° (Stalling):

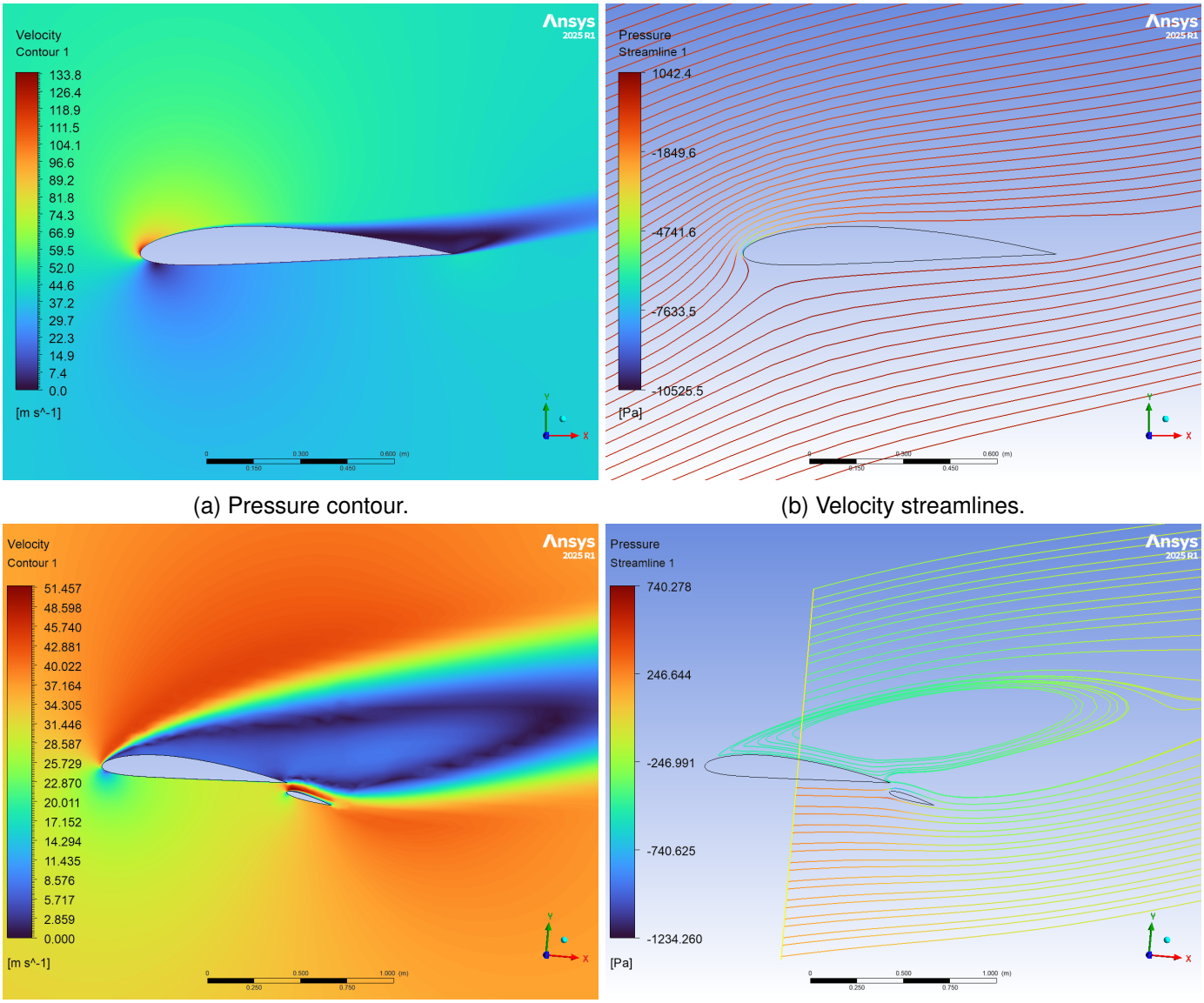

(a) Pressure contour.

(b) Velocity streamlines.

(c) Pressure contour.

(d) Velocity streamlines.

Figure 5: Simple and flapped aerofoils positioned at 16°.

At α = 16°, both aerofoils are clearly stalling. The pressure streamlines and velocity contour show a large separated region over the upper surface, with low speed and some reverse flow. The streamlines roll into a recirculation bubble rather than smoothly cascading off the trailing edge. The lower surface remains mostly attached. This separation indicates a loss of lift and increase in drag, as reflected in the data at this angle for both aerofoils.

At these angles of attack, the residuals did not converge for either case. The simple aerofoil did reach some degree of convergence for the drag and lift forces (462 iterations), however force results for the flapped aerofoil produced a considerable amount of variance and did not converge. This is very likely due to the mesh not being refined enough.

4 Results (Force Coefficient)

The thickness and camber ratio used to calculate the Joukowski and thin aerofoil conditions was 0.12.

$$\textbf{Thin Aerofoil: } C_L = 2\pi\alpha \qquad \textbf{Joukowski: } C_L = 2\pi(1 + 0.77\frac{t}{c})\sin(\alpha) \tag{5}$$

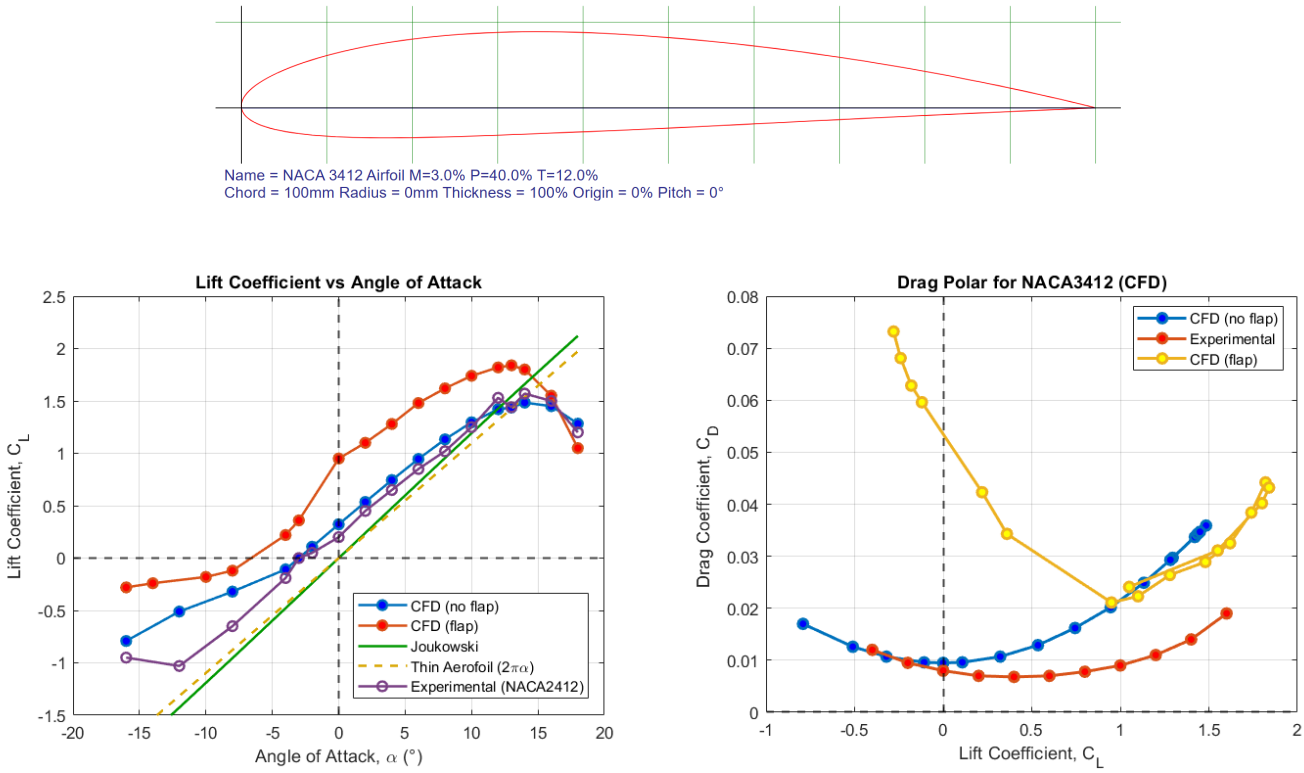

Figure 6: Lift Coefficient vs Angle of Attack and Drag Polar plots.

5 Assessment

While the results from this CFD simulation are reasonably accurate, there is clear room for improvement. The simple aerofoil produced much more stable and consistent results than the flapped case. To increase confidence in both sets of results, the mesh should be refined until some degree of mesh independence is achieved, i.e. further refinement does not significantly change C_L or C_D. In the flapped case, the relatively coarse mesh led to more scatter in the data and poorer resolution of pressure gradients, separation and the wake, so those results are less reliable.

No formal mesh- or domain-independence study was carried out, so the solution may still be influenced by grid density and the distance of the farfield boundaries. The simulations were also run using steady conditions with a fully turbulent assumption. In reality, the flow near stall is unsteady and the boundary layer is usually partially transitional, so this setup is likely to wrongly predict drag and slightly shift the lift curve. The calculations for drag can also be affected massively if a large amount of reverse flow occurs through flow separation.

The CFD was compared against experimental data for an aerofoil with 1% less camber, and the data were not taken directly from a table but from a plotted curve. This introduces extra uncertainty. Despite this the CFD results could be verified to some degree as the general trend agreed well, and the CFD consistently predicted slightly higher lift than the experiment. This makes sense as a greater camber would result in more lift being generated.

References

[1] SimuTech Group. Airfoil simulation in ansys fluent (naca 2412 tutorial). YouTube video, 2022. [cited 2025 Nov 10].

[2] Ansys Learning Channel. Ansys fluent meshing tutorial – airfoil cfd setup (naca 2412). YouTube video, 2023. [cited 2025 Nov 10].

[3] AirfoilTools. Airfoil comparison. Website, 2025. c2007–2025 [cited 2025 Nov 10].

[4] Cadence Design Systems, Inc. y-plus (y+) in cfd. Website, 2025. [cited 2025 Nov 10].